Beach-scale tidal variations observed from satellite-derived shoreline time series

Michael Hart-Davis
michael.hart-davis@tum.de
Technical University of Munich https://orcid.org/0000-0001-9342-0335
Thomas Monahan
Kilian Vos
Ole Andersen
Technical University of Denmark https://orcid.org/0000-0002-6685-3415

Article

Keywords:

Posted Date: March 15th, 2026

DOI: https://doi.org/10.21203/rs.3.rs-8967674/v1

Additional Declarations: There is **NO** Competing Interest.

Beach-scale tidal variations observed from satellite-derived shoreline time series

M.G. Hart-Davis[1*], **T. Monahan**[2], **K. Vos**[3], **and O. Andersen**[4]

[1]Deutsches Geodätisches Forschungsinstitut, Technische Universität München, Munich, Germany
[2]Department of Engineering Science, University of Oxford, Oxford, UK
[3]OHB, Bremen, Germany
[4]DTU Space, Technical University of Denmark, Kongens Lyngby, Denmark
Corresponding author(s): M. Hart-Davis (michael.hart-davis@tum.de)

ABSTRACT

Coastal tidal dynamics play a crucial role in a variety of biogeophysical processes, ranging from compound flooding to sediment transport. Satellite altimetry has revolutionized our understanding of ocean tides, but coastal regions remain challenging for satellite altimetry-based observations. In recent years, important efforts have been made to produce shoreline measurements from satellite optical imagery. These datasets raise the question of whether shoreline observations can resolve tidal dynamics at fine coastal scales. We show shoreline measurements provide fine-scale insights into tidal characteristics. Our results are contrasted with *in situ* measurements and state-of-the-art models as well as with wide-swath satellite observations. We explore how both harmonic analysis and response-based methods can be applied to these data to study a range of tidal constituents, including the phase-locked solar constituent S_2. Based on the extended time series, trends and changes in the M_2 constituent are estimated using shoreline observations and a variational Bayesian harmonic estimator. Our results show statistically significant trends around New Zealand, which are consistent with those estimated from *in situ* and altimetric observations. We demonstrate that satellite-derived shoreline measurements are a valuable resource for tidal research, particularly for model validation and the study of tidal constituent variability in the coastal zone.

Ocean tides are a significant driver of ocean circulation, with their influence being amplified in coastal regions. Coastal communities have studied and explored ocean tides for centuries due to their vast importance[1], particularly for compound flooding[2], fishing, and navigation. *In situ* tide gauges have historically been the main source of knowledge of ocean tides, especially in the coastal region[3]. While high-frequency temporal observations from gauges are a valuable resource, their coverage is spatially sparse, with only a small fraction of gauges in the global south. The spatial density of gauges makes fine-scale variability in the tides challenging to study.

In this context, satellite altimetry has revolutionized ocean tide research. The inclusion of altimetry resulted in significant increases in model accuracy across the global oceans[4]. As the altimeter time series continues to grow and coverage increases with new missions, the avenues of research on tides continue to grow, e.g., the study of tidal changes[5,6], shallow-water tides, or third-degree tidal constituents[7]. Particularly, the launch of the SWOT satellite, which observes a two-dimensional ocean surface[8], has opened the door to advanced studies of ocean tides across the land-ocean continuum[9,10]. Despite ocean tides having been studied for centuries, it is now evident that many avenues of research remain underexplored, particularly in the coastal zone.

Recent advances in satellite-derived shorelines (SDS) from optical satellites have enabled mapping of changes in shoreline position at unprecedented regional spatial scales and multi-decadal timescales[11,12]. These SDS methods leverage the long-term global archives of optical satellite imagery to automatically extract the position of the waterline at sub-pixel resolution on individual cloud-free images[13,14]. The output of these tools is a set of waterlines that represent the instantaneous boundary between water and land, modulated by the tides, as the satellite images are captured across different tidal phases. Thus, in order to use the waterlines as a coastal change indicator, they need to be post-processed into "shorelines". This is done by applying a tidal correction, using available tidal and beach slope information to reference the waterlines to a common vertical datum, essentially removing the tidal signal from the observations[15,16]. Yet, the tidal signal contained in the waterlines, which is generally treated as unwanted noise in shoreline change applications, contains valuable information about tidal dynamics at the coast. In this paper, we propose to isolate that tidal signal to estimate local tidal characteristics, effectively *turning someone's noise into someone else's signal*.

The advances in satellite-derived shoreline processing and datasets provide a tempting resource for the estimation and study of tidal variability at finer scales than previously possible. This is particularly true because these observations extend back to the mid-1980s, providing a long data record that can be exploited. The most obvious drawback is that these datasets quantify shoreline position and not sea-level; thus, the corresponding sea-level relative to the vertical datum must be inferred using knowledge of the beach slope. Additional difficulties arise in tidal research, as the orbits of these imagery satellites are sun-synchronous. Consequently, we cannot resolve the major solar components directly using conventional methods, which are an important factor in the full tidal signal (more on this later). If these imagery data can be used to estimate the other major tidal components, they will be a remarkable resource for understanding the small-scale variability of tides and could even aid in assessing the accuracy of global tide models.

In this manuscript, we evaluate the ability to obtain high-resolution tidal signals using shoreline measurements derived from satellite imagery. Two of the most commonly used methods for tidal analysis are explored: the harmonic method[17] and the response method[18] to provide insights from methods with varying applicability and strengths for tidal research. We contrast our findings with *in situ* tide gauges, global tide models, as well as high-resolution estimations we derive from the SWOT satellite. We additionally discuss new insights that can be observed about the spatial variability of ocean tides at finer spatial scales along the coasts, as well as provide a tentative assessment of long-term changes in the amplitude of the M_2 constituent as observed using these data.

Deriving Tides from satellite-derived shorelines

To a beach-goer, the movement of the waterline can be quite drastic within a matter of hours, largely thanks to the diurnal and semi-diurnal variations of the ocean tides. Therefore, the continued measurement of the waterline position presents an exciting opportunity for tidal research. However, the satellites from which these measurements are provided (Landsat[19]) have a repeat of 16 days, well above the frequencies of the semi-diurnal and diurnal tidal components driving the tide. Despite this unfavourable sampling, several major tidal components remain comfortably resolvable due to tidal aliasing[20]. As a result, the largest tidal constituent, M_2, which drives the two highs and two lows observed across most coastlines, is resolvable with just 191 days of Landsat measurements. The extended time-series, sometimes exceeding 40 years, additionally aids in combating issues of cloud cover that could cause breaks in the measurements or aid in separating non-tidal effects that could affect tidal estimation, especially in shorter time-series.

To start, a regional discussion of the tidal estimations from satellite-derived shorelines is contrasted with the FES2022 tide model ([21] updated) and *in situ* tide gauge measurements across New Zealand for both the harmonic and response method (Figure 1). By applying two different analysis methods, we can validate this measurement technique; if effective, both should consistently resolve the tidal components. For details on the methods used, readers are referred to the Methods section. New Zealand is selected due to data availability and because this region has relatively large tides, which means it has the greatest potential from a signal-to-noise perspective. Additionally, the tidal dynamics are unique around New Zealand, with tides propagating around the two main islands and large amplitude and phase-lag variations observed along the coastline.

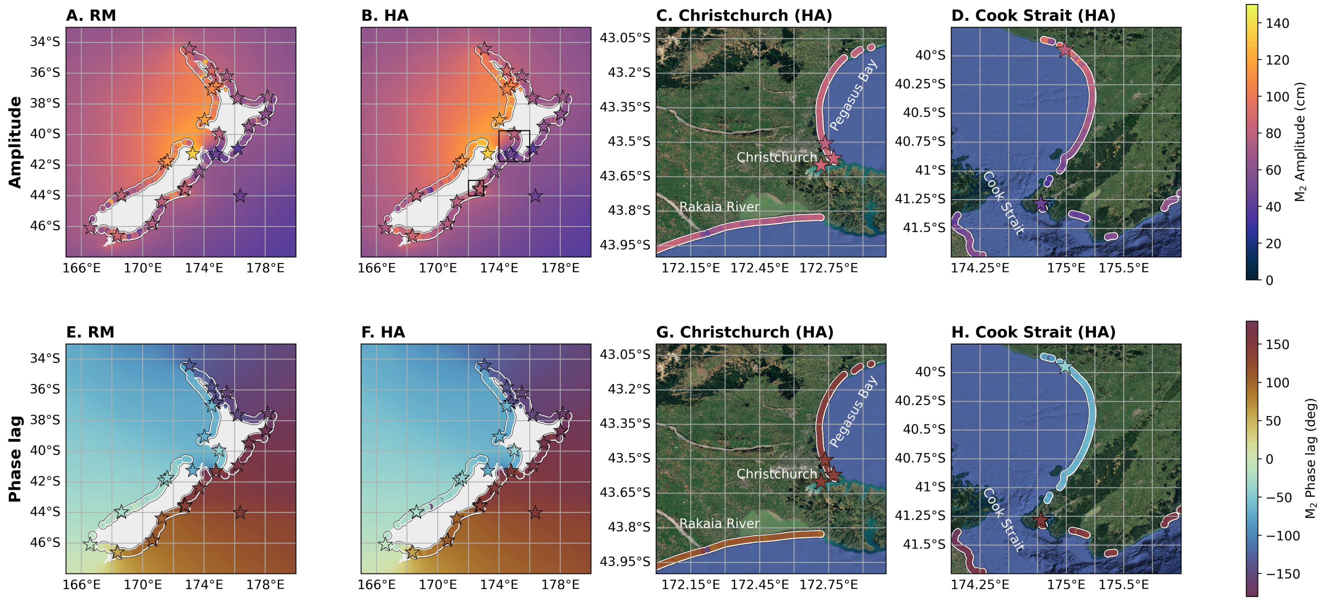

Figure 1. Shoreline-based predictions of the M_2 tidal constituent for both amplitude (top) and phase lag (bottom). A and E are estimates from the Response Method (RM), while the remaining estimates are made with a harmonic analysis (HA). The shoreline-based predictions are superimposed across the coasts, with the ocean covered by FES2022b predictions. Scarcely shown stars are *in situ* gauges around New Zealand. C and G present a zoom into Christchurch, and D and H present a zoom into the Cook Strait. Both regions are illustrated with a black box in B.

For New Zealand, both the harmonic and response methods produce amplitude and phase lag estimates that align visually and statistically; the differences are 2.36 cm (2% difference) and 2.05 deg on average between the approaches. Given that these observations are independent of the gauge and model being contrasted, the visual correlation of the M_2 tidal constituent estimates is clear. In Figure 1, the propagation of the M_2 along the entire coastline of New Zealand, shown in the phase lag, is well captured by the shoreline estimations, while the appropriate increases and decreases in amplitude match those of both the gauges and FES2022. The consistency between the methods and these independent sources provides the first confirmation that the shoreline data can be used to derive tidal estimates. Quantitatively, contrasting the methods with *in situ* measurements reveals amplitude errors of 5.77 cm and 7.74 cm, noting that tides exceed 1 meter in parts of the coast, as well as phase lag errors of 4.07 degrees and 8.29 degrees, for the harmonic and response method, respectively. When contrasting this to state-of-the-art altimetry-driven ocean tide models, which have amplitude errors of $\approx$2.5 cm and $\approx$1.5 degrees with respect to the same tide gauges, these results are quite promising. Direct comparisons with the FES2022 and GOT5.5[22] models show median differences of 3.1 cm and 6.6 degrees for the M_2 along the coast of New Zealand.

The zoom-in on Christchurch shows how shoreline-derived estimates match tide gauge observations, underscoring their value for tidal research. We can see that over small scales, like within the bays, the amplitude and phase lag of the tide are relatively stable for the M_2 constituent. Within the Bay to the north of Christchurch, Pegasus Bay, an amplitude increase from north to south of 5 cm is observed, while a phase decrease of 2 degrees is seen. For amplitude, this is just below 10% of the observed tide. To many applications, these fine variations may seem rather negligible, but this is nevertheless an interesting observation. From a tide modelling perspective, the model resolution is clearly an important factor in the accuracy and validation of models at the coast. Canterbury Bay (south of Christchurch) exhibits a 10 cm amplitude change over a 1-degree section of the beach.

Another interesting region from a tidal perspective is the Cook Strait between the islands of New Zealand. This is because this is an amphidromic point in the M_2, i.e. a point around which the tidal wave rotates and a region of near-zero amplitude. Both sides of the islands show low amplitudes in this region. Impressively, the shoreline measurements also capture the sharp change in phase lags, with the southern part of the North Island showing 220-degree phase changes in a 16 km stretch of coastline, as confirmed by tide gauges in the region. State-of-the-art models, as seen in Figure 1, do capture this process well, but with this increased spatial coverage, we can potentially better understand the physical structure of this amphidromic point, its fine spatial variability, and, therefore, the implications on the coastal zone.

In Figure 1C and F, a sharp change in the amplitude and phase lag can be observed at the mouth of the Rakaia River (south-west of the plot). These changes may be produced by several effects. First, rivers can drastically alter beach morphology, which may lead to major changes in beach slope estimation. Second, rivers present a challenge for automated shoreline detection algorithms as, at different stages of the tide, water may flow continuously from river to sea without presenting a clear shore-break. Further challenges may occur as a result of the complex interaction of river dynamics and tidal dynamics, causing aliasing effects in the tidal estimation[23,24]. The unprecedented spatial resolution that we are able to obtain from these data highlights these effects. Hence, to provide a suitable comparison with the global models when expanding to the full Pacific region (Figure 2), we removed any observations from our dataset within 1 km of a river mouth, and in the *in situ* comparison, we excluded tide gauges labelled ‘river’. For the model analysis, this resulted in the removal of nearly 550 shoreline observations in our study area, with negligible changes in the median statistics.

The estimations across the Pacific region are shown in Figure 2 for the harmonic estimation and in Extended Data Figure 1 for the response method. When evaluating the estimates, the qualitative comparisons of both the amplitude and the phase lag of the M_2 remain rather impressive. This is further quantified in comparisons to both tide gauges and global tide models. In Figure 3, the harmonic method is compared to two state-of-the-art tide models, FES2022 and GOT5.5. These models are widely used across a variety of applications and provide insights into current modelling capabilities. The amplitude differences are relatively low throughout, with the mean being around 3.1 cm for both models. The phase lags are also small in most regions of the Pacific Ocean, except for the northern section of Peru and the southern section of North America. On average, the phase lags vary by 6.70 degrees and 6.62 degrees for FES2022 and GOT5.5, respectively. The root-mean-square (RMS) is 7.534 and 7.538 cm, respectively, for FES2022 and GOT5.5. In Extended Data Table 1, the mean statistics of five tidal constituents are compared. As the shoreline imagery data dates back to the mid-80s, the main reason for the interest in analyzing this dataset is that the effect of aliasing and noise is expected to be reduced, particularly from non-tidal effects. However, we anticipate that some aliasing effects from local wave activity may be stronger in some constituents and regions. For the M_2 tide, as well as the N_2 and K_2 tides (shown in the Extended Data Figure 3), the amplitude of these tides exceeds 10s of centimeters throughout our domain. This means the tidal analysis is less influenced by non-tidal processes, such as waves. This is confirmed by the validation, with smaller errors observed from these semi-diurnal tides compared to both models and *in situ* measurements.

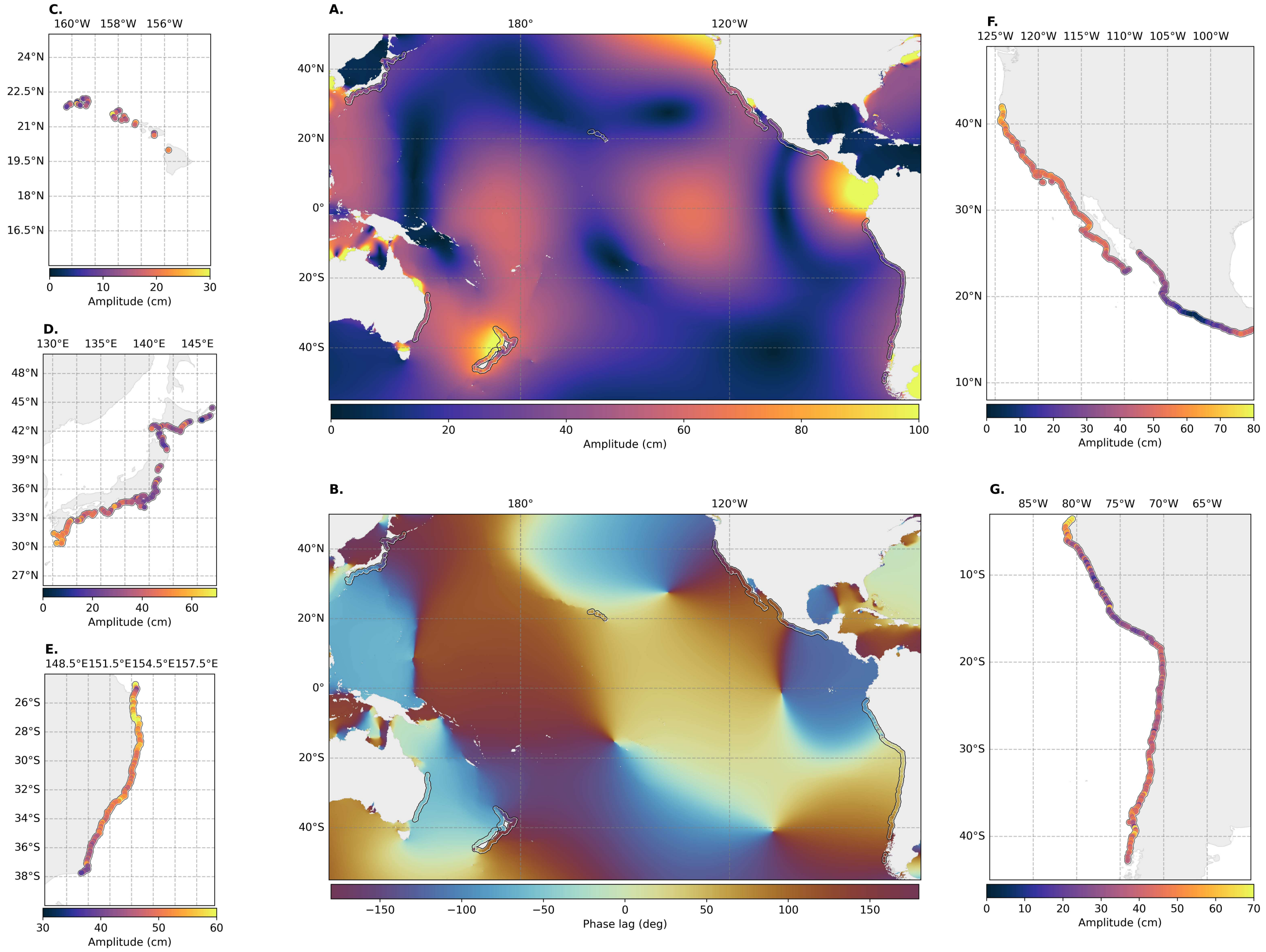

Figure 2. Satellite imagery-based predictions of the M_2 tidal constituent for both amplitude (A) and phase lag (B) derived from the harmonic analysis, with zooms added of regions observed in the dataset for clarification. New Zealand is withheld from the regional zooms to avoid duplication of Figure 1. The ocean is covered by FES2022b predictions. Full results of the response method are presented in Extended Data Figure 1.

In Figure 3G and H, the RMS error of the shoreline-derived tides using the harmonic and response estimations is compared to tide gauges. The RMS of the harmonic approach shows median errors of 9.42 cm, whereas the response method yields an RMS of 10.78 cm. These results are solid, but differences occur between these two methods. On inspection, these differences are likely due to how the two methods handle the separation of tidal constituents and the noise inherent to the data. While prior work has shown that the response method yields results comparable to (and in some cases slightly better than) harmonic analysis across various conditions[18], the shoreline observations pose a unique challenge for a fully automated global procedure (which we employ). First, there is a large range of tidal variability across different regions, and thus, using a fixed selection of lags can produce suboptimal results. Second, we do not utilize Radiational input functions. This choice was deliberate as the sparsity of the data makes estimation of the additional weights challenging. However, this may be compensated for by the gravitational response estimate, potentially degrading estimates of pure gravitational constituents.

While the results of this analysis may not be as accurate as those from satellite altimetry in the open ocean or from tide gauges along the coast, the value of this dataset is highlighted in regions with limited or no *in situ* observations. For example, in our analysis, the coast of South America is observed by only 9 tide gauges, meaning that modelling efforts cannot capture small-scale variations in the tide. However, using these results, we can see that the models are doing a rather reasonable job at modelling the tidal variations in these regions (Figure 3). The expansion of shoreline imagery datasets to the global coasts, or at least critical coastal regions, such as the Arctic coast and the coasts of Africa, where *in situ* observations are severely lacking, will not only benefit the shoreline community but also the tidal community.

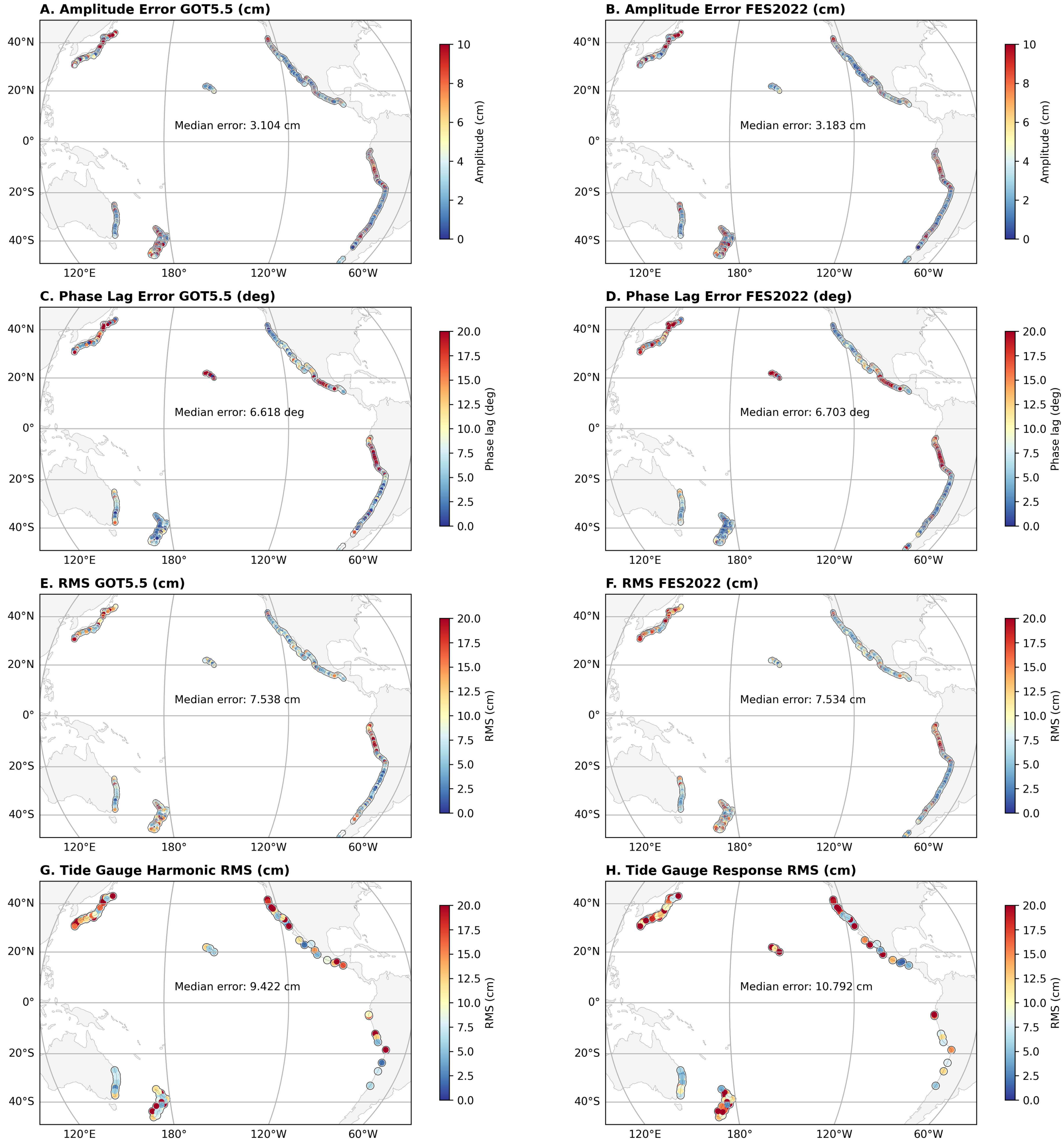

Figure 3. Amplitude, phase lag, and RMS error of the harmonic analysis shoreline measurements compared to two state-of-the-art global ocean tide models (GOT5.5 and FES2022) for the M$_2$ constituent. The bottom row presents the RMS error of the harmonic and response method-derived shoreline estimations compared to TICON-4.

Other constituents

The diurnal tides, on the other hand, are significantly smaller, barely exceeding 10 centimeters for a majority of the coastlines. Using a harmonic analysis, O$_1$ is the largest diurnal tide we can solve for reliably, but, as shown in the Appendix, it never exceeds 5 cm along the coastlines we evaluate. Based on the horizontal uncertainty in shoreline estimates of about 10 meters and median slopes of 6 cm in our study region, using a 10 cm threshold is equivalent to considering only constituents with a median signal-to-noise ratio (SNR) of > 1.4. As shown by[25], even if this error is perfectly Gaussian, unregularised ordinary-least-squares harmonic estimators will begin to be biased below 0 SNR.

Hence, when we apply this threshold to our analysis, only comparing tides greater than 10 cm, our results for all constituents in both amplitude and phase lag differences are improved (contrast Appendix Table 1 and 2). A more extensive description of the uncertainties is presented in the Section "Tentative estimates of tidal trends". Based on these conservative signal-to-noise restrictions, despite O_1 being technically resolvable, we would not use it any further in our analysis. Hence, we conclude the major semi-diurnal tides can be reliably used and interpreted from shoreline imagery as is, while the diurnal tides require special treatment before they are reliably useful for tidal research. For a discussion on P_1 and K_1 see methods.

The S_2 tide

The sun-synchronous orbit renders the estimation of solar tides impossible using a standard harmonic analysis. This is a consequence of the solar tides being sampled at the exact same phase at each pass. When discretizing into individual tidal lines, this leads to an infinite aliasing of the solar tides. In contrast, a response-based analysis does not discretize the tidal response into individual lines. Instead, it defines a smooth admittance function over neighbouring frequencies. The fact that we can estimate neighbouring constituents (previously discussed), combined with the smoothness of the response admittance, allows us to estimate solar tides. We further generalize this approach to implicitly account for the spatial coherence of neighbouring shoreline observations by introducing a generalized coupled response method. The results shown use this approach, and a description of the method is provided in the Methods. Examples of estimated S_2 amplitudes around New Zealand are shown in Figure 4 with FES2022 shown in the background and individual gauges overlaid. Several insights can be gleaned from this. On the western shore of the island, which is characterized by a larger S_2 amplitude (> 25 cm on average), the response estimated S_2 amplitudes and phases are both in good agreement with both FES2022 and the *in situ* gauges.

In contrast, the Eastern side of the island is characterized by much lower amplitudes (< 10 cm on average). In this region, the estimated response amplitudes are larger than those observed. The phase estimates are reasonable in the South Eastern arm, but are considerably off moving up to the North East corner. Inspection of the pseudo-admittances of the TICON-4 gauges indicates that it is likely not a consequence of strong resonances (see Extended Data Figure 2). This is further confirmed by the fact that the response amplitudes and phases show good agreement with the gauge located in the Cook Strait, which exhibits a strong non-equilibrium relationship between S_2 and the rest of the semi-diurnal band. Instead, we speculate that the observed inaccuracy is more likely a function of the signal-to-noise ratio. In a response approach, the admittance function defines a *smooth* relationship between closely spaced frequencies[18]. While the complexity of this function is defined by the lags employed for the analysis, the function itself can be thought of as a data-driven interpolation between closely spaced frequencies. A challenge with this is that other semi-diurnal constituents, such as K_2 and N_2, which help define the admittance function over the semi-diurnal band, have small magnitudes in many regions. Hence, the smoothness of the admittance, which in many contexts is the strength of the response approach, can actually be biased by poor estimates of the smaller segments of the semi-diurnal band. In our testing, phase estimates appeared to be more resilient to such biasing.

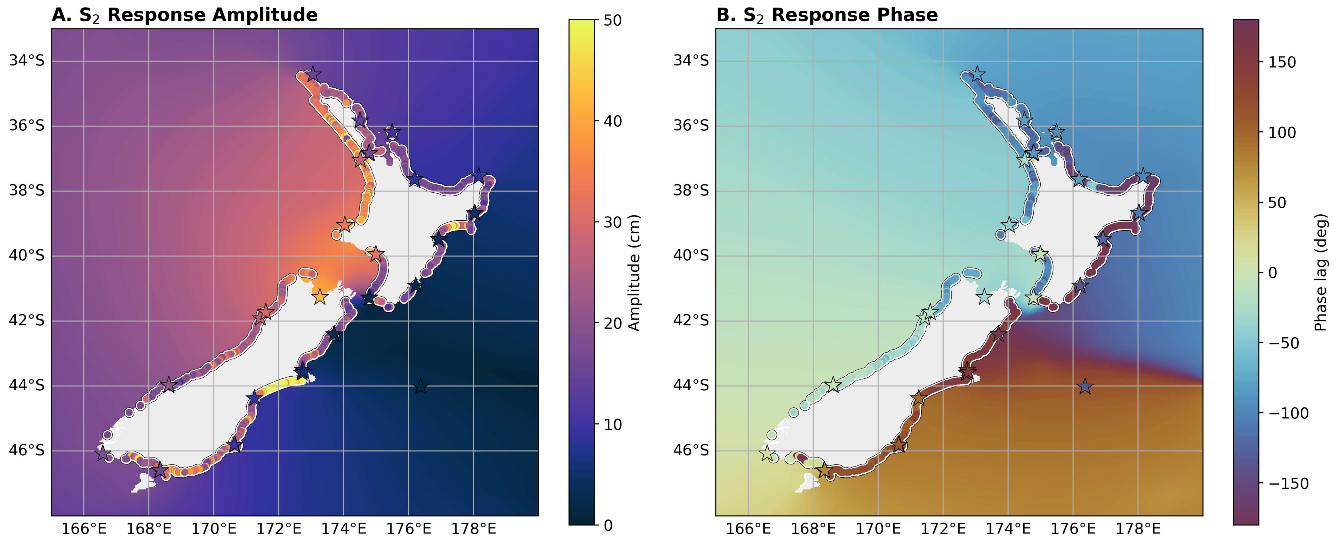

Figure 4. S_2 tide from the response method compared to tide gauges and the FES2022 model.

Tentative estimates of tidal trends

The long time series of shoreline data and the demonstrated ability to resolve the major M_2 tide pose the question as to whether observations can be made about tidal changes. In recent years, several model-based studies (e.g.[26–28], tide gauge-based studies (e.g.[29,30]) and more recently, altimetry-derived studies (e.g.[5,6]) have demonstrated that tidal constituents themselves are experiencing changes resulting from human-based activity (e.g. human-induced climate change, coastline reclamation, to name a few). While deriving such trends from the shoreline data may be challenging due to non-tidal effects, we present a tentative look at derived tidal trends below. In our analysis, the results are compared to tide gauge-based trends derived from[3] and altimetry-based trends derived from[6].

Several caveats should be noted before a deeper discussion of the accuracy of trend estimates from each method. This mainly stems from the sensitivity of tidal trends, which are typically very small relative to the signal, to data quality and changes in data. For tide gauge trends, local changes, such as shifts in gauge position and data quality, can result in significant changes in trend estimates. While the data from[3] uses 'research quality' data from UHSLC `https://uhslc.soest.hawaii.edu/` that aims to reduce several of these effects, effects may still cause issues in the tidal trend estimations. Satellite altimetry-derived trends have several issues, largely driven by the accuracy of the satellite data and by geophysical corrections (see[6] for a detailed explanation). Additionally, altimetry-derived trends usually rely on the Topex/Poseidon, Jason, and Sentinel-6 satellites, resulting in coarse resolution in the estimates; the data product from[6] has a 0.5-degree resolution. In contrast, shoreline observations present several new uncertainties not encountered with conventional altimetry. First, a key parameter used when estimating waterlines from satellite imagery is the beach slope. Here, we treat the beach slope as constant because of the limited availability of time-series data on beach slopes. However, beach slopes can change due to coastal erosion and human activity, leading to errors in estimations. These changes manifest as large annual fluctuations in mean shorelines and can thus be filtered out to some extent (see Figure 5).

A comparison of trends from the shoreline data is given in Figure 5. The geographical distribution of shoreline estimates, gridded altimetry estimates, and gauges is shown in the left panels for each region. In the right panels, we plot the distributions of shoreline estimates with gauges overlaid. If we first consider the shoreline points in the left panels, we observe spatially coherent trends in most regions. By spatially coherent, we refer to clusters of points with similar colours (trend magnitudes). If we consider these trends to be accurate, this demonstrates that, while trends may behave in spatially coherent ways, there is significant variance at the finer scale. Such variance is likely not captured by analysis of conventional altimetry, and is also challenging to assess using conventional tide-gauges due to their sparsity. We look to compare the observed regional shoreline trends with gauge-estimated trends in the corresponding histograms. The mean and standard deviations are reported for both gauge and shoreline trends and are computed using an inverse-variance weighting (IVW) scheme. This approach ensures that observations with lower formal uncertainties contribute more significantly to the regional average.

To correctly account for the disparity in sample sizes and the presence of any unmodeled physical dispersion, we apply a variance scaling factor (reduced χ^2) to the IVW uncertainty (See methods). This formulation prevents the high-frequency sampling of the satellite data from artificially deflating the uncertainty, providing a conservative and statistically sound basis for comparing the satellite-derived trends against the sparse but high-precision tide gauge network. The lack of spatial dependence in this calculation may overestimate the effective sample size. The asterisks next to the shoreline estimates indicate whether or not the regional trend is statistically significantly different from those estimated from the gauges. It can be seen that for New Zealand, Australia, Mexico, and Peru, the observed trends are statistically consistent with those estimated from gauges. As observed in conventional altimeters, simulations, and gauge observations, New Zealand exhibits large negative trends. Our regional estimates indicate the mean trend in New Zealand is < -1.0 mm/year at the 68% credible level, and < 0.82 mm/year at the 95% credible level (See methods for a note on credible vs. confidence intervals). Other regions with smaller trends prove less conclusive using the present approach.

Peru, for instance, appears to have a positive trend if we consider the overlap between 68% and 95% credible intervals. However, the magnitude of that trend varies between 0.25 mm/year and 2.69 mm/year at the 95% credible level. Hence, few insights can be gleaned from these estimates other than that prior estimates from altimetry of a slight positive trend are broadly in agreement. Nearby in Chile, we observe similarly large positive trends of 1.61 mm/year on average, this time with much tighter credible intervals. Due to the sparsity of gauges in the region (n=3 gauges), and the larger estimate from a single gauge of over 10 mm/year, gauge estimates have a 95% credible interval spanning +/- 3 mm/year. As such, the shoreline observations provide strong evidence of a positive trend in the region. For the remaining regions, Japan and California, we observe trends which are statistically significantly different from the gauges at the 95% credible level. For both locations, the gauge estimated trends are less than 0.3 mm/year. We observe good coherence between the histograms of the shoreline estimates and the point estimates from the gauges in the central quartile of the distributions. However, the heavier and asymmetric tails associated with the shoreline distributions induce a bias of the means. Future work is warranted in understanding whether these tail characteristics over a region are endemic to tidal change, or rather an artefact of errors produced by the shoreline trend estimates (see discussion below).

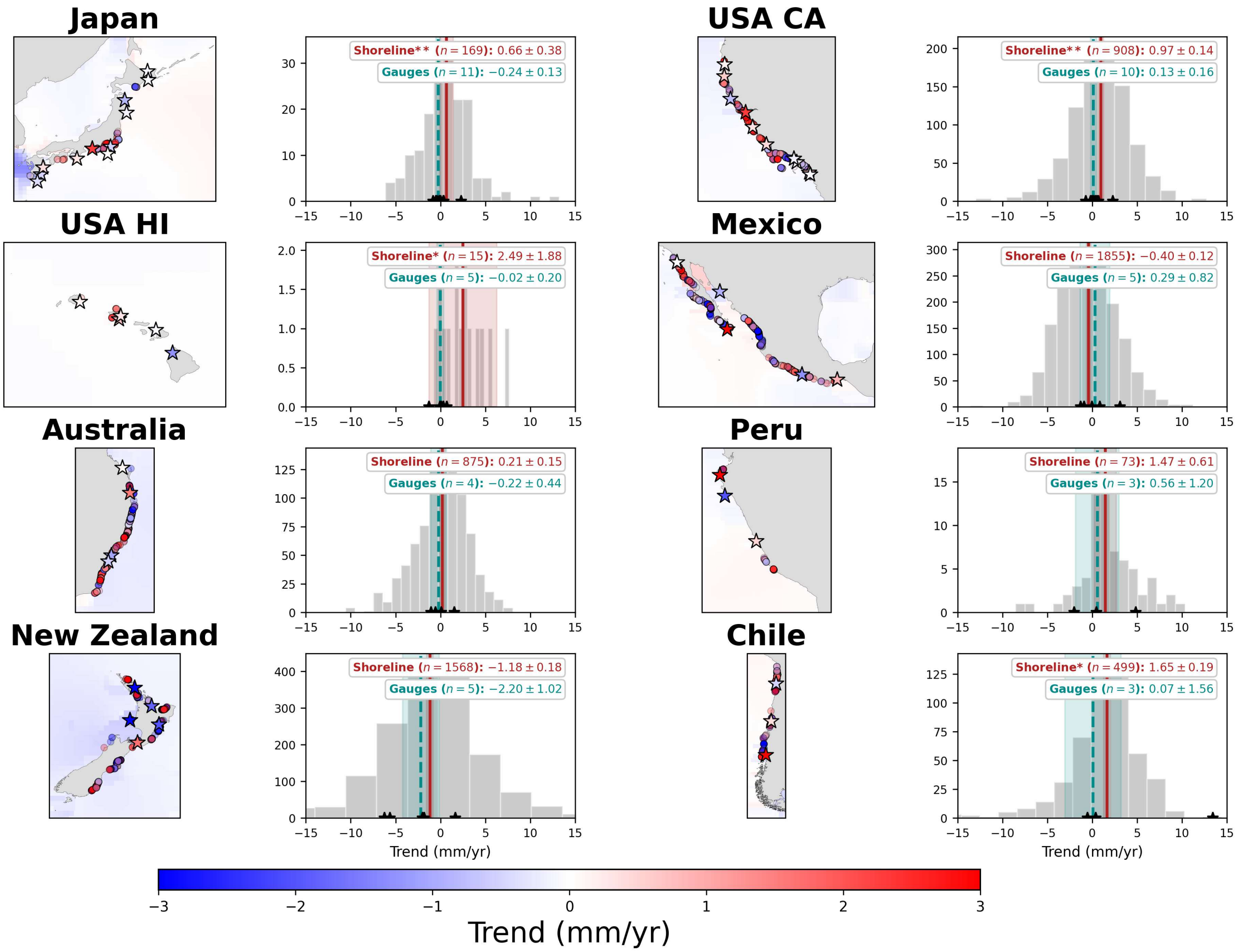

Figure 5. Trends in M_2 tidal constituents through the different regions. Maps show shoreline estimated trends with gauge trends given by stars and altimetry-derived estimates over the ocean. Panels display regional maps (left) alongside their corresponding trend distributions (right). In the maps, pixels represent shoreline-estimated trends, while stars indicate localized tide gauge trends. Histograms illustrate the frequency distribution of shoreline observations, with individual gauge trends marked by stars along the x-axis. Reported values include the inverse-variance weighted (IVW) means and robust uncertainties for both datasets. Significance levels for the disparity between shoreline and gauge observations are denoted next to the shoreline mean: a single asterisk ($*$) indicates a difference exceeding the 1σ level (68% credible), while double asterisks ($**$) denotes a significant difference at the 2σ level ($\approx$ 95% credible) under a Gaussian assumption.

In total, in 5 out of 8 regions, we observe non-zero trends at the 95% credible level. While the M_2 constituent estimates appear robust, the observed trends are orders of magnitude smaller. As such, large variations in beach slope, potentially from anthropogenic or environmental factors, can significantly impact downstream trend estimates. Two primary factors were identified in many of the time series of the anomalous trends produced: limited data and/or significant non-stationarity in the annual mean sea levels. With regard to the former, we pre-filter the data to remove long-term sea-level trends, and to remove outliers by first filtering out sea-levels greater than or less than 5 meters and then remove observations exceeding +/- 3 standard deviations of the mean. On the other hand, large changes in annual mean sea levels on the order of meters are likely a consequence of changing beach morphology and not a reflection of sea-level processes[15]. To avoid bias from these data, we restrict our trend estimates to time series that have greater than 450 observations and a maximum change in annual mean sea levels of less than 1.5 meters over the observation period. Both values were determined empirically through extensive inspection of individual time series and trend estimates.

Comparison with wide-swath altimetry

Global tide models, despite reaching high resolutions, typically rely on conventional along-track nadir altimeters to derive tidal estimations. In late 2022, the SWOT satellite launched which has already provided novel insights into tidal variability thanks to its unique two-dimensional measurement technique[8]. Several sea surface height products are available from SWOT, ranging from 2 km in the open ocean up to 50 meters in inland waters. In this section, the M_2 is derived from the 2 km product to provide an additional independent comparison to the shoreline estimations (Figure 6). These estimations were done on the sea-level anomaly (SLA), withholding any tidal corrections, so that the SWOT estimation is a full tidal estimation. We again focus on a regional assessment around New Zealand due to the complexity of the tidal system as well as due to data availability. Research on the estimation of tides from SWOT itself is in its infancy, but early research has hinted at large potential, particularly in resolving tides in the coastal regions[9,25,31]. Qualitatively, the results of tidal estimation from SWOT around New Zealand matches the estimations made by global tide models (see Figure 1). In the Cook Strait, the 250-meter product is used to compare with the M_2 and demonstrate its high spatial variability.

Compared to *in situ* gauges, SWOT shows an error of 3.5 cm and 7.8 degrees for the M_2 tide. These findings are particularly impressive when one considers that global model errors in the region of 2.37 cm and 4.47 degrees from the GOT5.5 model, despite SWOT having provided global data for only approximately 3 years. Additionally, SWOT estimates and shoreline estimates, such as those from global models, correlate well along the New Zealand coastline. The differences are calculated to be 4.46 cm and 5.69 degrees between these two methods in this region. SWOT is currently the only satellite measurement technique that allows such near-coastal estimations of ocean tides, but it has only operated since 2022. While this satellite and its processing continue to improve, an exciting potential may be in the combination of these two approaches or the results of these approaches to derive tidal estimates throughout the coastal zone to allow for the derivation of a large number of tidal constituents, including the solar tides, thanks to the non-sun-synchronous orbit of SWOT. As seen in the Cook Strait, the amphidromic point is well observed from SWOT (alongside the shoreline measurements), which also opens the door for the finer structure of this region to be studied to potentially further describe the physical structure of this amphidromic point, as well as its impact on the coastal dynamics in the surrounding region.

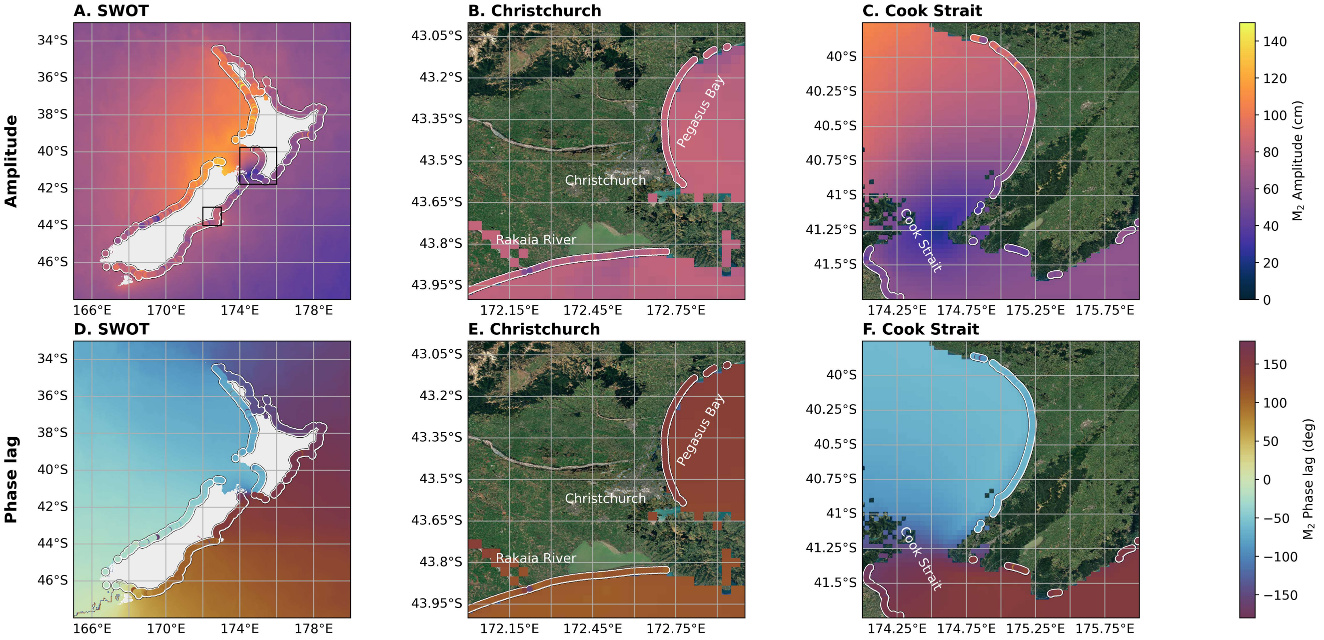

Figure 6. The amplitude and phase lag of the M_2 tidal constituent derived from SWOT and the shoreline imagery. Shoreline estimates are outlined in white. Two regional assessments are presented around Christchurch and the Cook Strait

Conclusion

Through this research, we demonstrate that novel insights into tidal dynamics can be obtained from shoreline imagery. Particularly strong results are obtained in the largest tidal constituent, M_2, where our estimates closely match those made by *in situ* observations, tide models, and wide-swath observations. The beach-scale variability of tidal constituents provides valuable insights into tides in coastal regions, where tides are increasingly significant to coastal communities, particularly in the context of compound flooding.

What is particularly useful about these data is their independence compared to global models and *in situ* gauges. This presents the opportunity to provide a new validation resource that can aid in the understanding of global modelling errors, which is vital for several downstream applications, particularly for sea level measurements from altimetry. The findings presented in the Pacific Ocean demonstrate how we can fill the gaps in our *in situ* tide gauge coverage for this validation. The expansion of these data to the global coasts, or at least poorly observed coastlines, is, therefore, clearly important for not only understanding shoreline variability but also for tidal research across these regions. This will be further improved with increased temporal coverage of shorelines, as well as the continued extension of these datasets and the refinement of processing strategies to reduce errors and uncertainties in estimates. These factors will expand the usability of these data for tidal research, particularly into further tidal constituents. A logical follow-up is also the evaluation of tidal estimates from shorelines derived from PlanetScope satellites, which provide higher spatial and temporal resolution[32] and could aid in refining tidal estimation accuracy and expanding to more tidal constituents.

The long record of observations presents another potential resource for evaluating how tides are changing at a much longer temporal scale than conventional altimetry. Our tentative assessment of M_2 tidal trends from shoreline imagery shows coherence with previous literature using tide gauges and *in situ* observations. While there may be systematic errors that create uncertainty in the estimates, this preliminary research highlights an interesting avenue for research that theoretically can be expanded to the global coasts. The success of these future studies will rely on reducing the potential sources of uncertainty in our estimates, namely, the usage of a fixed beach slope. Future work may therefore consider using non-parametric approaches, such as Gaussian Processes, to simultaneously estimate a time-variable beach slope alongside tidal constituents. The launch of wide-swath altimetry will clearly be a vital resource for coastal tidal research. However, this record is considerably shorter than that provided by shoreline imagery. Therefore, a further avenue of research could be in the development of methods or the use of machine learning algorithms to merge these observation types. This is particularly crucial for the solar constituents, which can be resolved by the SWOT satellite.

Methods

CoastSat satellite-derived shorelines

The satellite-derived shoreline data used in this work are based on the long-term CoastSat multi-decadal shoreline dataset for the Pacific Rim (1984 to 2026), publicly available on Zenodo (v1.5 https://zenodo.org/records/14889613). The dataset integrates imagery from the Landsat missions (1984-present, Landsat 5, 7, 8 and 9) across wave-dominated coastlines in the Pacific Basin (Australia, New Zealand, Japan, Hawaii, California, Mexico, Peru, Chile). CoastSat[33] derives time series of shoreline positions by detecting the instantaneous water-sand interface on individual optical satellite images. For each available, cloud-free satellite image, shorelines are mapped using the Modified Normalized Difference Water Index (MNDWI) combined with supervised image classification of the scene into water, whitewater, sand, and other land-cover classes. An image-specific Otsu threshold is then applied to delineate the waterline along the water-sand boundary using a marching-squares sub-pixel resolution contouring algorithm[34]. Individual waterline detections are then intersected with shore-normal transects spaced at 100 m intervals to produce cross-shore position time series. In the data repository, both waterline position time series and tidally-corrected shoreline position time series are provided, but for this work, only the waterlines are used (i.e. *timeseries_raw.csv* in the repository). The horizontal accuracy of sub-pixel resolution waterlines extracted from Landsat imagery is of the order of 5 m[35]. As the waterlines are transformed into shoreline positions, additional sources of error are introduced (beach slope, water level), leading to typical root-mean-square horizontal accuracies of approximately 8-12 m for satellite-derived shorelines when validated against *in situ* beach topographic surveys[36]. The CoastSat data are routinely updated (`https://zenodo.org/records/4760144`) and openly available at `http://coastsat.space`.

An important clarification regarding the waterline data: the CoastSat shoreline dataset also provides FES2022 time series for users to apply as a tidal correction to their waterline observations. We do not use these observations in our study and only evaluate the uncorrected waterline observations. Additionally, the single value of beach-face slope provided for each transect is used to convert the horizontal waterline positions into vertical water levels. This may cause confusion that the time-series would be influenced by the tidal correction; however, this beach slope estimate is a fixed, singular estimate that does not change throughout the time-series in which the tidal analysis is performed. This means that the uncorrected observations we are using are independent of any tide model.

Table 1. Aliasing period (in days) of the major eight tidal constituents based on the repeat orbit of Landsat.

Constituent	Aliasing period (in days)
M_2	191.336878
S_2	∞
K_2	182.621095
N_2	47.659970
K_1	365.242190
O_1	125.560418
P_1	365.242190
Q_1	54.812363

Tidal analysis

On these collected observations, tidal analysis is done using a harmonic and response method. The harmonic method was developed in the 1800s and is the most widely used method in tidal research (see[17,37] for detailed discussions). In this study, we use the TICON software[38] to conduct the harmonic analysis to resolve the amplitude and phase lag of the tidal constituents studied (M_2, K_2, N_2, O_1, and Q_1). One may note that three so-called 'major' tides are missing, P_1, K_1, and S_2 from the harmonic analysis. This was based on the aliasing of these constituents. For each tide, the aliasing period is shown in Table 1. For the K_1 and P_1 tides, their frequencies get aliased onto the same period, 365.25 days. This means that in fact these two tidal constituents are not separable from one another as well as they are aliased onto the annual cycle based on the sampling of Landsat, meaning we cannot derive these two constituents. The S_2 tide itself is aliased to infinity because of the sun-synchronous orbit, resulting in the S_2 wave being sampled at the same phase of the tide. This means from a purely harmonic analysis, the S_2 is not resolvable. However, a dedicated discussion is presented in the manuscript on S_2 attempting to resolve this tide using the response method.

Classical response method

Following Munk & Cartwright[18], tidal variability is modeled as the linear, time-invariant response of the ocean to the astronomical tidal potential. The gravitational potential is expanded in spherical harmonics, yielding complex input functions $c_n^m(t)$. The predicted signal at a given location is expressed as a convolution over discrete time lags $\{\tau_s\}$,

$$\hat{y}(t) = \sum_{m,n}\sum_{s}\left[x_n^m(s)\,a_n^m(t-\tau_s) + y_n^m(s)\,b_n^m(t-\tau_s)\right], \tag{1}$$

where a_n^m and b_n^m are the real and imaginary components of the tidal potential, and $x_n^m(s), y_n^m(s)$ are learned response weights. In the frequency domain, this corresponds to estimating the complex tidal admittance via cross-spectral analysis. In practice, weights may also be obtained through time-domain least-squares regression. The response estimated S_2 in Extended Data Figure 2 uses this standard formulation and lag-based implementation of the response method.

Coupled Response Method

A challenge with the shoreline observations is that they are both temporally sparse and can be quite noisy. This presents a signal-to-noise ratio (SNR) problem. One approach to improve the SNR is by considering multiple transects simultaneously e.g. assuming the response is spatially coherent over a region. To achieve this, we adopt a data-driven non-parametric formulation that retains the response-method framework (forcing → time-invariant mapping) while allowing the interactions to be learned directly from the data. This network-based approach follows from[39,40]. Furthermore, the notion of defining spatially coherent response functions traces back to suggestions from Cartwright and Ray in their work on Geosat[41]. The following formulation can be seen to take inspiration from this approach without imposing stringent assumptions on the nature of these spatial relationships other than that they come from a coupled set of weights, and they are spatially "similar" (more on this to follow).

Let $\mathbf{V}(t)$ denote the vector of gravitational input functions evaluated at selected time lags. Instead of predicting a single scalar response, we model N shoreline transects simultaneously:

$$\hat{\beta}(t) = f\big(\mathbf{V}(t-\tau_1),\ldots,\mathbf{V}(t-\tau_S)\big), \tag{2}$$

where

$$\hat{\beta}(t) = \left[\hat{\beta}_1(t),\ldots,\hat{\beta}_N(t)\right]^{\top}$$

represents shoreline position (or elevation-equivalent response) at N transects, and $f(\cdot)$ is a shared neural network.

In contrast to the coupled current model of Monahan et al. (2025b), which produces two outputs (u, v), here the final layer contains N linear outputs, allowing the network to learn both: (i) the mapping from forcing to response, and (ii) spatial coupling between transects through shared hidden layers.

Architecture and training. The model is a fully connected feed-forward neural network with 3 hidden layers and tanh activation functions. The output layer is linear with N nodes. Inputs and targets are standardized prior to training.

Weights are estimated via gradient descent by minimizing a composite loss function,

$$\mathscr{L} = \mathrm{MSE}_{\mathrm{NaN}} + \lambda \mathscr{L}_{\mathrm{smooth}}, \tag{3}$$

where the NaN-aware mean squared error is

$$\mathrm{MSE}_{\mathrm{NaN}} = \frac{1}{|\Omega|} \sum_{(i,t)\in\Omega} \left(\beta_i(t) - \hat{\beta}_i(t)\right)^2, \tag{4}$$

with Ω the set of valid (non-missing) observations.

Spatial coherence is enforced through a smoothness penalty across neighboring transects,

$$\mathscr{L}_{\mathrm{smooth}} = \frac{1}{N} \sum_i \frac{1}{|\mathscr{N}(i)|} \sum_{j\in\mathscr{N}(i)} \left(\hat{\beta}_i - \hat{\beta}_j\right)^2, \tag{5}$$

where $\mathscr{N}(i)$ denotes the set of spatial neighbors of transect i, determined using k-nearest neighbors in geographic space. The hyperparameter λ controls the strength of spatial regularization. While this method is a step beyond the original response method, the formulation preserves the physical interpretation of a time-invariant mapping from tidal forcing to sea-level response while generalizing it to a spatially coupled, multi-output shoreline system. By virtue of training on exclusively shoreline observations, the results reflect what can be obtained from shoreline observations.

Bayesian Trend Estimation

To estimate tidal trends we assume the quadrature tidal amplitudes vary linearly in time similar in spirit to the TintHA approach[42]. Unlike TintHA, which parameterizes linear evolution of the complex harmonic constant over a fixed analysis window and reports the associated startâĂŞend change, we model linear trends in the real quadrature components within a variational Bayesian regression and derive instantaneous amplitude rates (per year) via explicit transformation and covariance propagation. Consequently, our shoreline trend estimates are expressed directly as continuous rates with posterior-consistent uncertainty, whereas TintHA trends are framed as window-relative changes. These modifications are reflective of the challenges of working with the shoreline data and the need for consistent error propagation and internal uncertainty estimates. The advantage of this approach is that we do not need to break the record up into chunks, which would introduces aliasing challenges due to the sparse temporal sampling of the shoreline observations. The disadvantage is that this approach imposes an assumption of a linear trend, which may be incorrect. Given we compare these trends to other workers who assume linearity, we feel this assumption is necessary and sufficient.

Let $y(t_i)$ denote observed sea level at times t_i ($i = 1, \ldots, N$). The tidal signal is represented as a linear superposition of K harmonic constituents with time-varying quadrature coefficients,

$$y(t_i) = \sum_{k=1}^{K} \left[a_k(t_i)\, \phi_k(t_i) + b_k(t_i)\, \psi_k(t_i)\right] + \beta\, \tau_i + \varepsilon_i, \tag{6}$$

where ϕ_k and ψ_k are the cosine and sine basis functions for constituent k (including nodal corrections), $\tau_i = (t_i - t_{\mathrm{ref}})/365.2425$ is centred time in years relative to the record midpoint t_{ref}, β is a linear mean sea-level trend, and $\varepsilon_i \sim \mathscr{N}(0, \sigma^2)$.

To allow linear changes in constituent amplitude, quadrature coefficients are parameterised as

$$a_k(t) = a_{k0} + a_{k1}\tau, \qquad b_k(t) = b_{k0} + b_{k1}\tau. \tag{7}$$

Stacking all regressors yields the linear model

$$\mathbf{y} = \mathbf{X}\mathbf{w} + \varepsilon. \tag{8}$$

Parameters are estimated using variational Bayesian linear regression with automatic relevance determination (ARD) shrinkage ([25]). Gaussian priors are placed on regression weights with Gamma hyperpriors on their precisions and on the noise precision. A complete description of this approach, and direct comparisons with ordinary least-squares and other regularized least-squares estimators is provided in that manuscript. Our approach is also available in the open-source VTide Python package (`https://github.com/thomasmonahan/VTide`)

The variational posterior provides a Gaussian approximation

$$p(\mathbf{w} \mid \mathbf{y}) \approx \mathcal{N}(\mu, \mathbf{V}), \tag{9}$$

yielding posterior means and the full covariance matrix $\mathbf{V}$.

At the reference epoch, constituent amplitude and phases are recovered by

$$A_{k,\mathrm{ref}} = \sqrt{a_{k0}^2 + b_{k0}^2}, \qquad \varphi_{k,\mathrm{ref}} = \tan^{-1}\left(\frac{-b_{k0}}{a_{k0}}\right). \tag{10}$$

The linear amplitude rate (per year) is then calculated as

$$\dot{A}_k = \frac{a_{k0}a_{k1} + b_{k0}b_{k1}}{A_{k,\mathrm{ref}}}. \tag{11}$$

Uncertainties in amplitudes and amplitude rates are obtained via first-order error propagation using the full posterior covariance $\mathbf{V}$ (delta method). Specifically, for a differentiable function $g(\mathbf{w})$ of the regression parameters $\mathbf{w}$ with posterior mean μ and covariance $\mathbf{V}$, the variance is approximated as

$$\mathrm{Var}[g(\mathbf{w})] \approx \nabla g(\mu)^\top \mathbf{V} \nabla g(\mu), \tag{12}$$

where ∇g denotes the gradient with respect to $\mathbf{w}$. For $A_{k,\mathrm{ref}}$ and $\dot{A}_k$, gradients are evaluated analytically with respect to $(a_{k0}, b_{k0}, a_{k1}, b_{k1})$, ensuring that covariance between quadrature coefficients is fully retained.

Predictive uncertainty combines observation noise and parameter uncertainty as

$$\mathrm{Var}[y_*] = \sigma^2 + \mathbf{x}_*^\top \mathbf{V} \mathbf{x}_*, \tag{13}$$

where σ^2 is the posterior mean noise variance and $\mathbf{x}_*$ is the design vector at time t_*. These uncertainties are then combined using an inverse variance weighting procedure in Figure 5.

For each site $i = 1, \ldots, n$, let $\widehat{\dot{A}}_{k,i}$ denote the posterior mean amplitude rate for constituent k, and let $\sigma_{k,i}$ denote its corresponding posterior standard deviation obtained via the delta method described above. We form the inverse-variance weighted (IVW) regional mean trend

$$\widehat{\dot{A}}_{k,\mathrm{reg}} = \frac{\sum_{i=1}^n w_{k,i} \widehat{\dot{A}}_{k,i}}{\sum_{i=1}^n w_{k,i}}, \qquad w_{k,i} = \frac{1}{\sigma_{k,i}^2}. \tag{14}$$

The nominal internal uncertainty of the IVW estimator is

$$\sigma_{k,\mathrm{int}} = \left(\sum_{i=1}^n w_{k,i}\right)^{-1/2}. \tag{15}$$

To account for excess dispersion across sites relative to their reported posterior uncertainties, we compute the reduced chi-square statistic

$$\chi_{\nu,k}^2 = \frac{1}{n-1} \sum_{i=1}^n w_{k,i} \left(\widehat{\dot{A}}_{k,i} - \widehat{\dot{A}}_{k,\mathrm{reg}}\right)^2, \tag{16}$$

and inflate the regional uncertainty as

$$\sigma_{k,\mathrm{reg}} = \sigma_{k,\mathrm{int}} \sqrt{\max\left(1, \chi_{\nu,k}^2\right)}. \tag{17}$$

Credible vs. confidence intervals Due to the assumptions made by our variational Bayesian estimator, the uncertainty estimates presented come from an assumed Gaussian posterior distribution. The intervals shown are *credible* intervals, meaning they represent the range of parameter values that contain a given fraction (e.g. 68% or 95%) of posterior probability under the assumed model. Under the Gaussian approximation used here, these intervals coincide numerically with the familiar $\pm 1\sigma$ and $\pm 2\sigma$ uncertainty bounds often interpreted as 68% and 95% confidence intervals, but their interpretation is probabilistic rather than purely frequentist

Comparative tidal datasets

Tide gauge observations were obtained from the TICON-4 dataset (Hart-Davis et al 2025), which provides tidal constituents derived from the GESLA-4 dataset (Haigh et al 2022, updated). All available tide gauges from the Pacific Ocean were used to validate the shoreline estimations, totaling 559 gauges. Our estimations were additionally compared to three tide models: GOT5.5[22] and FES2022[21]. For each of these models, the respective tidal constituents were sampled at the same location as the shoreline imagery and used for comparisons.

Wide-swath altimetry

The Surface Water and Ocean Topography (SWOT) satellite is a wide-swath altimeter that enables the resolution of two-dimensional ocean and inland waters[8]. In this study, the L2 ocean product obtained from PODAAC (https://doi.org/10.5067/SWOT-SSH-D) is used, which provides along-track observations of sea level anomalies (SLA) at 2 km spatial resolution. The SLA data are obtained from the $ssha-karin-2$ variable, which we do not correct for the ocean tides to enable full tidal estimation. For the regional analysis, all L2 SWOT observations are collected from 2023 to January 2026 for the New Zealand domain. A regional grid at 2 km is then created, from which each SWOT pass is regridded. This allows the creation of a product containing all observations of a specific grid point across all passes, resulting in a time series of SLA from which harmonic analysis can be conducted. We run the same harmonic analysis as done in the shoreline observations, except only resolving the M_2 tidal constituent for the purposes of the discussions within the manuscript.

Data availability

The CoastSat satellite-derived shoreline dataset is publicly available on Zenodo at https://zenodo.org/records/4760144 (v1.5 was used for this study) and can be visualised interactively at http://coastsat.space. The TICON-4 tide gauge dataset can be found at: https://doi.org/10.17882/109129. The FES2022 model is available at https://www.aviso.altimetry.fr/en/data.html, while GOT5.5 is available at https://earth.gsfc.nasa.gov/geo/data/ocean-tide-models.

Code availability

The RTide software to produce the tidal analysis can be found here: https://github.com/thomasmonahan/RTide. Code to replicate the shoreline measurements can be found at: https://github.com/kvos/CoastSat.

References

1. Cartwright, D. E. *Tides: A Scientific History* (Cambridge University Press, Cambridge, 1999). 292pp.
2. Li, S. *et al.* Compounding of Sea-Level Processes During High-Tide Flooding Along the U.S. Coastline. *Journal of Geophysical Research: Oceans* **128**, e2023JC019885 (2023). URL https://agupubs.onlinelibrary.wiley.com/doi/abs/10.1029/2023JC019885. E2023JC019885 2023JC019885.
3. Hart-Davis, M. G. *et al.* Tide of the Time: Global tidal characteristics observed from in-situ measurements (2026). URL http://dx.doi.org/10.5194/egusphere-2026-346.
4. Stammer, D. *et al.* Accuracy assessment of global barotropic ocean tide models. *Reviews of Geophysics* **52**, 243–282 (2014). URL https://agupubs.onlinelibrary.wiley.com/doi/abs/10.1002/2014RG000450.
5. Bij de Vaate, I., Slobbe, D. C. & Verlaan, M. Secular trends in global tides derived from satellite radar altimetry. *Journal of Geophysical Research: Oceans* **127**, e2022JC018845 (2022). URL https://agupubs.onlinelibrary.wiley.com/doi/abs/10.1029/2022JC018845. E2022JC018845 2022JC018845.
6. Ray, R. D. & Schindelegger, M. Trends in the M_2 ocean tide observed by satellite altimetry in the presence of systematic errors. *Journal of Geodesy* **99** (2025). URL http://dx.doi.org/10.1007/s00190-025-01935-9.
7. Ray, R. D. First global observations of third-degree ocean tides. *Science Advances* **6**, eabd4744 (2020).
8. Fu, L.-L. *et al.* The Surface Water and Ocean Topography mission: A breakthrough in radar remote sensing of the ocean and land surface water. *Geophysical Research Letters* **51**, e2023GL107652 (2024). URL https://agupubs.onlinelibrary.wiley.com/doi/abs/10.1029/2023GL107652. E2023GL107652 2023GL107652.
9. Hart-Davis, M. G. and Andersen, O. B. and Ray, R. D. and Zaron, E. D. and Schwatke, C. and Arildsen, R. L. and Dettmering, D. and Nielsen, K. Tides in Complex Coastal Regions: Early Case Studies From Wide-Swath SWOT Measurements. *Geophysical Research Letters* **51** (2024). URL http://dx.doi.org/10.1029/2024GL109983.

10. Hart-Davis, M. and Scherer, D. and Schwatke, C. and Sawyer, A. and Pavelsky, T. and Ray, R. and Dettmering, D. and Seitz, F. Observing the pulse of tidal rivers: A first global analysis from wide-swath satellite altimetry (2026). URL `10.21203/rs.3.rs-6825606/v1`.

11. Warrick, J. A. *et al.* Net widening of Southern California beaches. *Nature Communications* (2026).

12. Vos, K., Harley, M. D., Turner, I. L. & Splinter, K. D. Pacific shoreline erosion and accretion patterns controlled by El Niño/Southern Oscillation. *Nature Geoscience* **16**, 140–146 (2023).

13. Sanchez-Garcia, E. *et al.* An efficient protocol for accurate and massive shoreline definition from mid-resolution satellite imagery. *Coastal Engineering* **160**, 103732 (2020). URL `https://www.sciencedirect.com/science/article/pii/S0378383918306070`.

14. Vos, K., Harley, M. D., Splinter, K. D., Simmons, J. A. & Turner, I. L. Sub-annual to multi-decadal shoreline variability from publicly available satellite imagery. *Coastal Engineering* **150**, 160–174 (2019).

15. Vos, K., Harley, M. D., Splinter, K. D., Walker, A. & Turner, I. L. Beach slopes from satellite-derived shorelines. *Geophysical Research Letters* **47**, e2020GL088365 (2020). URL `https://agupubs.onlinelibrary.wiley.com/doi/abs/10.1029/2020GL088365`. E2020GL088365 2020GL088365.

16. Konstantinou, A. *et al.* Satellite-based shoreline detection along high-energy macrotidal coasts and influence of beach state. *Marine Geology* **462**, 107082 (2023). URL `https://www.sciencedirect.com/science/article/pii/S0025322723000944`.

17. Doodson, A. T. The harmonic development of the tide-generating potential. *Proceedings of the Royal Society of London. Series A* **100**, 305–329 (1921).

18. Munk, W. H. & Cartwright, D. E. Tidal spectroscopy and prediction. *Philosophical Transactions of the Royal Society of London. Series A* **259**, 533–581 (1966).

19. Sheffner, E. J. The landsat program: recent history and prospects. *Photogrammetric Engineering and Remote Sensing* **60**, 735–744 (1994).

20. Parke, M. E., Stewart, R. H., Farless, D. L. & Cartwright, D. E. On the choice of orbits for an altimetric satellite to study ocean circulation and tides. *Journal of Geophysical Research: Oceans* **92**, 11693–11707 (1987).

21. Lyard, F. H., Allain, D. J., Cancet, M., Carrère, L. & Picot, N. FES2014 global ocean tide atlas: design and performance. *Ocean Science* **17**, 615–649 (2021). URL `https://os.copernicus.org/articles/17/615/2021/`.

22. Ray, R. D. Documentation for Goddard Ocean Tide solution GOT5: Global tides from multi-mission satellite altimetry. NASA Tech. Memo. 20250002085, Goddard Space Flight Center, Greenbelt MD (2025). URL `https://ntrs.nasa.gov/api/citations/20250002085/downloads/GOT5-TechMemo.pdf`.

23. Hoitink, A. J. F. & Jay, D. A. Tidal river dynamics: Implications for deltas. *Reviews of Geophysics* **54**, 240–272 (2016). URL `https://agupubs.onlinelibrary.wiley.com/doi/10.1002/2015RG000507`.

24. Matte, P., Jay, D. A. & Zaron, E. D. Adaptation of classical tidal harmonic analysis to nonstationary tides, with application to river tides. *Journal of Atmospheric and Oceanic Technology* **30**, 569–589 (2013).

25. Monahan, T., Tang, T., Roberts, S. & Adcock, T. A. Tidal corrections from and for SWOT using a spatially coherent variational Bayesian harmonic analysis. *Journal of Geophysical Research: Oceans* **130**, e2024JC021533 (2025).

26. Carless, S. J., Green, J. M., Pelling, H. E. & Wilmes, S.-B. Effects of future sea-level rise on tidal processes on the Patagonian Shelf. *Journal of Marine Systems* **163**, 113–124 (2016). URL `http://dx.doi.org/10.1016/j.jmarsys.2016.07.007`.

27. Haigh, I. D. *et al.* GESLA Version 3: A major update to the global higher-frequency sea-level dataset. *Geoscience Data Journal* **10**, 293–314 (2022). URL `http://dx.doi.org/10.1002/gdj3.174`.

28. Opel, L., Schindelegger, M. & Ray, R. D. A likely role for stratification in long-term changes of the global ocean tides. *Communications Earth amp; Environment* **5** (2024). URL `http://dx.doi.org/10.1038/s43247-024-01432-5`.

29. Ray, R. D. Secular changes in the solar semidiurnal tide of the western North Atlantic Ocean. *Geophysical Research Letters* **36**, L19601 (2009).

30. Woodworth, P. L. A survey of recent changes in the main components of the ocean tide. *Continental Shelf Research* **30**, 1680–1691 (2010).

31. Arildsen, R. L., Andersen, O. B., Nilsson, B. & Ludwigsen, C. B. Tidal bore revealed by SWOT: a case study from the Severn River. *Scientific Reports* **15** (2025). URL `http://dx.doi.org/10.1038/s41598-025-99597-2`.

32. Doherty, Y., Harley, M. D., Vos, K. & Splinter, K. D. A Python toolkit to monitor sandy shoreline change using high-resolution PlanetScope cubesats. *Environmental Modelling amp; Software* **157**, 105512 (2022). URL `http://dx.doi.org/10.1016/j.envsoft.2022.105512`.

33. Vos, K., Splinter, K. D., Harley, M. D., Simmons, J. A. & Turner, I. L. CoastSat: A Google Earth Engine-enabled Python toolkit to extract shorelines from publicly available satellite imagery. *Environmental Modelling & Software* **122**, 104528 (2019).

34. Cipolletti, M. P., Delrieux, C. A., Perillo, G. M. & Piccolo, M. C. Superresolution border segmentation and measurement in remote sensing images. *Computers & Geosciences* **40**, 87–96 (2012).

35. Pardo-Pascual, J. E., Almonacid-Caballer, J., Ruiz, L. A. & Palomar-VÃązquez, J. Automatic extraction of shorelines from Landsat TM and ETM+ multi-temporal images with subpixel precision. *Remote Sensing of Environment* **123**, 1–11 (2012). URL `https://www.sciencedirect.com/science/article/pii/S0034425712001174`.

36. Kras, E., Luijendijk, A. *et al.* Benchmarking satellite-derived shoreline mapping algorithms. *Communications Earth & Environment* **4**, 345 (2023).

37. Pugh, D. & Woodworth, P. *Sea-Level Science: Understanding Tides, Surges, Tsunamis and Mean Sea-Level Changes* (Cambridge University Press, 2014). URL `http://dx.doi.org/10.1017/CBO9781139235778`.

38. Hart-Davis, M., Dettmering, D. & Seitz, F. TICON-4: TIdal CONstants based on GESLA-4 sea-level records (2025).

39. Monahan, T., Tang, T., Roberts, S. & Adcock, T. A. RTide: Automating the tidal response method. *Journal of Geophysical Research: Machine Learning and Computation* **2**, e2024JH000525 (2025).

40. Monahan, T., Tang, T., Roberts, S. & Adcock, T. A. Response-based prediction of tidal currents. *Journal of Geophysical Research: Oceans* **130**, e2025JC022758 (2025).

41. Cartwright, D. E. & Ray, R. Oceanic tides from Geosat altimetry. *Journal of Geophysical Research: Oceans* **95**, 3069–3090 (1990).

42. Bij de Vaate, I., Slobbe, D. & Verlaan, M. Secular trends in global tides derived from satellite radar altimetry. *Journal of Geophysical Research: Oceans* **127**, e2022JC018845 (2022).

Acknowledgements

TM acknowledges support from the Eric and Wendy Schmidt AI in Science Postdoctoral Fellowship, a Schmidt Futures program. TM also acknowledges support from New College, University of Oxford.

Author contributions statement

MGHD conceptualized this study. MGHD and TM ran the tidal analysis. TM developed the methodology to analyse the tidal trends and solar tides, with input from MGHD and OA. MGHD and TM produced the figures for the manuscript. KV produced the shoreline measurement dataset for the tidal analysis. MGHD, TM, and OA wrote the first draft of this manuscript and analyzed the results presented. All authors reviewed and edited the paper.

Competing interests

All authors express no competing interests.

Extended Data

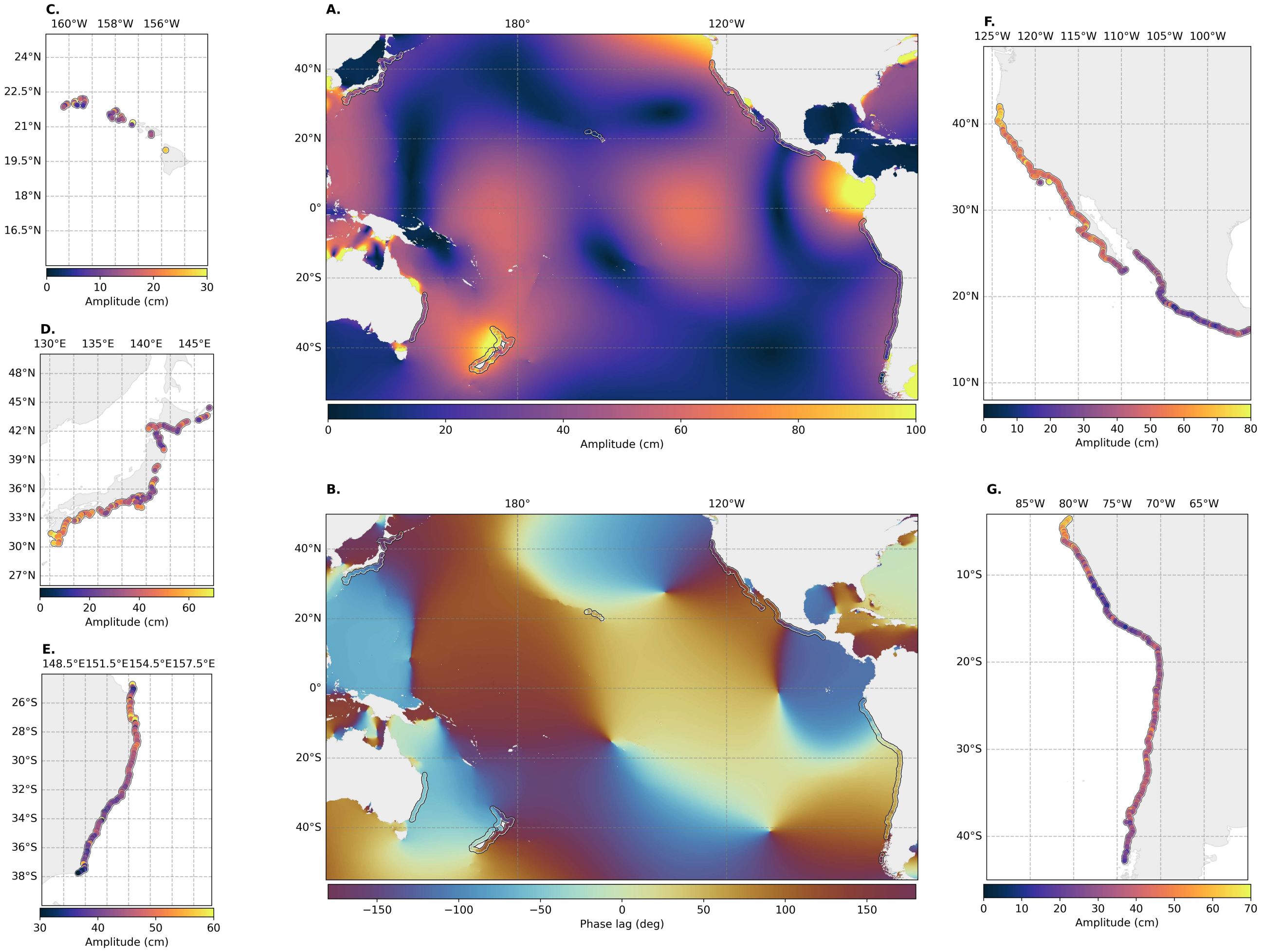

Extended Data Figure 1. Satellite imagery-based predictions of the M_2 tidal constituent for both amplitude (A) and phase lag (B) derived from the response method, with zooms added of regions observed in the dataset for clarification. New Zealand is withheld from the regional zooms to avoid duplication of Figure 1. The ocean is covered by FES2022b predictions.

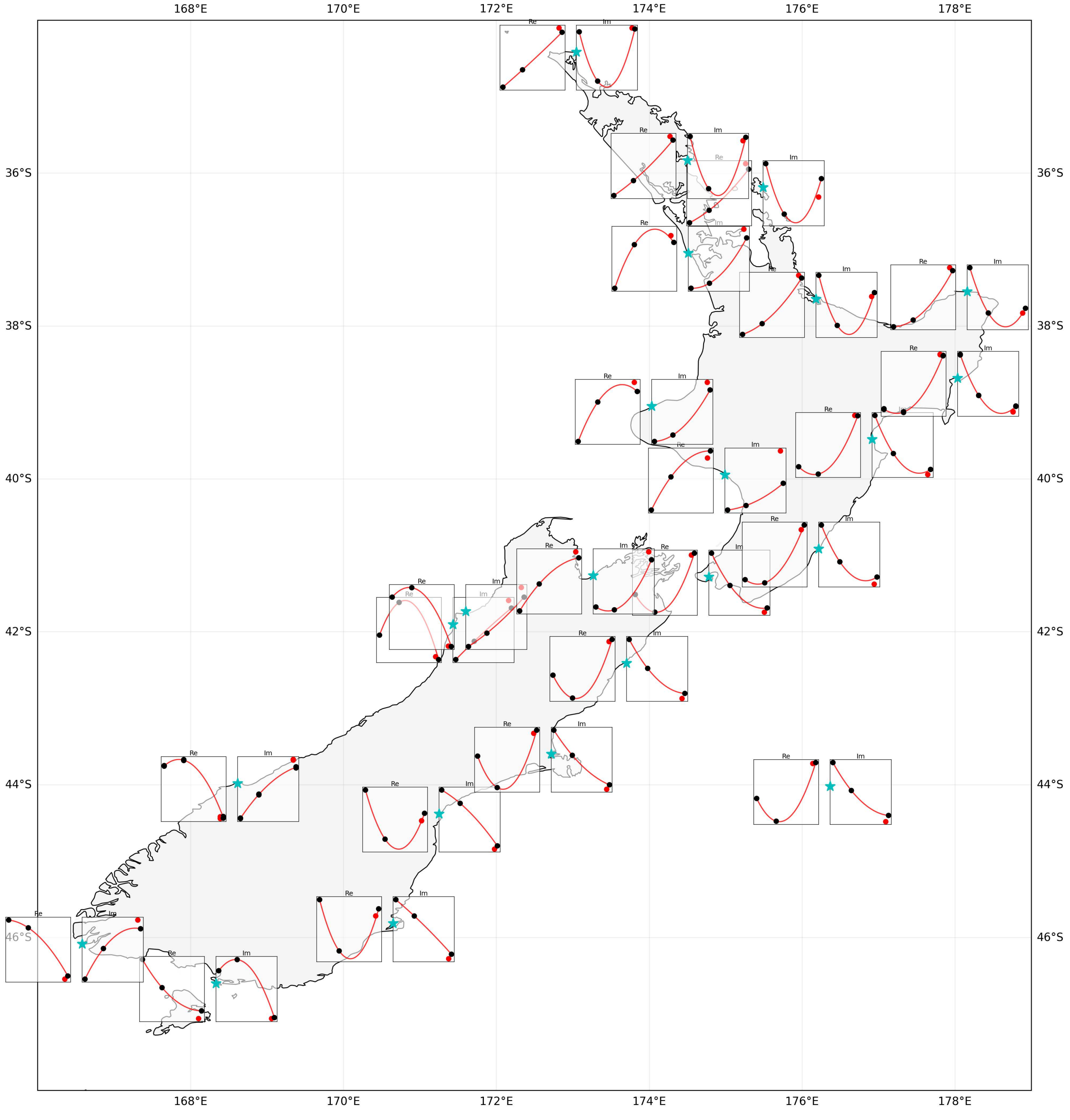

Extended Data Figure 2. Estimates of semi-diurnal pseudo-admittances from TICON-4 gauges. Estimates are made by fitting a 3rd degree polynomial to equilibrium normalized M_2, N_2, and K_2 tides. These are not true admittances but illustrate where large deviations of S_2 exist.

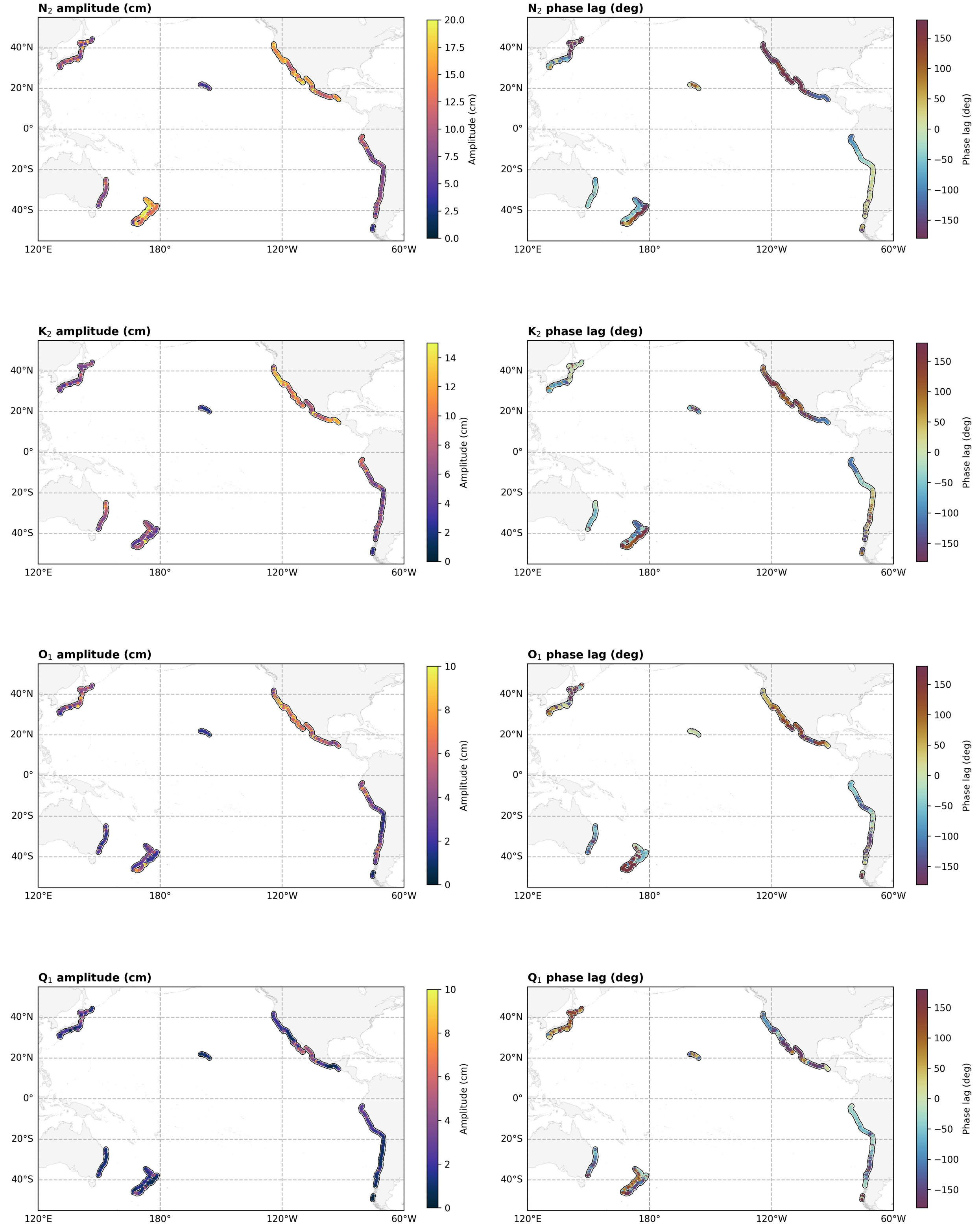

Extended Data Figure 3. Additional four tidal constituents across the Pacific coastlines derived from the harmonic analysis

Extended Data Table 1. Comparison of shoreline tidal constituent estimations using harmonic analysis with global tide models.

	Amplitude		Phase		RMS	
	FES2022	GOT5.5	FES2022	GOT5.5	FES2022	GOT5.5
M_2	4.777	4.727	6.685	6.796	9.240	9.159
N_2	3.428	3.391	14.481	14.057	5.625	5.621
K_2	12.692	12.627	108.266	107.095	18.059	18.772
O_1	4.456	4.439	19.317	17.184	7.010	7.088
Q_1	9.665	9.641	58.306	54.818	11.083	11.481

Extended Data Table 2. Comparison of shoreline tidal estimations with global tide models, with only regions where tidal amplitudes exceed 10 cm shown to reduce the impact of noise. Note that this threshold results in Q_1 being removed from the table.

	Amplitude		Phase		RMS	
	FES2022	GOT5.5	FES2022	GOT5.5	FES2022	GOT5.5
M_2	4.842	4.768	6.642	6.751	9.350	9.205
N_2	2.586	2.558	11.424	10.794	4.795	4.733
K_2	2.265	2.850	16.313	15.846	4.482	4.361
O_1	2.989	3.016	13.696	12.361	5.536	5.273